Evolution of Structure in the Incommensurate Modulated $LaNb_{1-x}W_xO_{4+x/2}$ (x = 0.04–0.16) Oxide Ion Conductors

Cheng Li,[1,2,3*] Stevin S. Pramana,[1,4] Ryan D. Bayliss,[1] Clare P. Grey,[5] Frédéric Blanc,[5,6] and Stephen J. Skinner[1*]

[1]Department of Materials, Imperial College London, Exhibition Road, London, SW7 2AZ, UK

[2]Jülich Centre for Neutron Science JCNS, Forschungszentrum Jülich GmbH, Outstation at SNS, Oak Ridge, TN 37831-6473, USA

[3]Neutron Scattering Division, Oak Ridge National Laboratory, Oak Ridge, TN 37831-6473, USA

[4]School of Engineering, Newcastle University, Newcastle upon Tyne, NE1 7RU, UK

[5]Department of Chemistry, University of Cambridge, Lensfield Road, Cambridge, CB2 1EW

[6]Department of Chemistry, Stephenson Institute for Renewable Energy, Crown Street, University of Liverpool, Liverpool, L69 3BX

*corresponding authors:

lic1@ornl.gov, tel +1 865 232 8422, address: 8600 Oak Ridge National Laboratory, 1 Bethel Valley Rd, Oak Ridge, TN 37830

s.skinner@imperial.ac.uk, tel +44 (0)20 7594 6782, address: Imperial College London, South Kensington Campus, London SW7 2AZ

Abstract

Hyper-stoichiometric $CeNbO_{4+d}$ phases demonstrate remarkable oxygen diffusivity and provide an interesting structural template for oxygen ion conductors. Previously, we have reported the room temperature structure of the incommensurate modulated $LaNb_{0.88}W_{0.12}O_{4.06}$, a structural analogue of $CeNbO_{4+d}$. We have confirmed that it is a pure oxygen ion conductor, with anions diffusing *via* an interstitialcy mechanism. However, the high temperature structural information for the $LaNb_{1-x}W_xO_{4+d}$ (x = 0.04 - 0.16) family, which is key to understanding the structure-property relationship in oxygen ionic conductors with complex structures at operating conditions, is unreported. In this contribution, we address this question by investigating the high temperature structural evolution of the $LaNb_{1-x}W_xO_{4+2/x}$ phases using a combination of thermal analysis, scattering techniques and ^{17}O and ^{93}Nb nuclear magnetic resonance spectroscopy. We reveal a series of phase transitions between a modulated monoclinic phase, a high temperature modulated tetragonal phase and a high temperature unmodulated tetragonal phase. These findings are correlated with the ion transport and offer insights into the design of new materials for solid state electrochemical devices.

1 Introduction

Discovery and optimization of ionic conducting electrolyte materials is crucial in obtaining solid oxide fuel cells (SOFCs) with lower operation temperature.[1–5] The established electrolyte materials are limited to fluorite and perovskite-based systems, which rely on an isotropic, vacancy hopping mechanism facilitated by the cubic or near cubic crystal lattice.[1–3]

Recent years however have witnessed a growing interest towards complex structures with anisotropic conducting pathways for electrolyte applications. The apatite[4,6] and the melilite[5,7] families for instance have shown high oxide ion conductivity (~0.001-0.01 S cm^{-1}) in the intermediate temperature range (500-700 °C).

Another family of interest is the hyper-stoichiometric fergusonite/scheelite structure which finds application in a wide range of electrochemical devices including fuel cells, electrolysers and permeation membranes.[8–11] Their unity oxide ionic transfer number, good thermal stability and high total electrical conductivity make them attractive alternatives to conventional materials (for instance, conductivity of $\sigma = 0.042$ S cm^{-1} at 800 °C was reported for the scheelite $Pb_{0.8}La_{0.2}WO_{4+d}$, comparable to that of the yttria stabilised zirconia, or YSZ, benchmark[10,12]). One member of the fergusonite/scheelite family, the hyper-stoichiometric $CeNbO_{4+d}$ phases have shown remarkable oxygen diffusivity, D^*, in the range of 10^{-6} cm^2 s^{-1}, below 800 °C, about an order of magnitude higher than the YSZ.[9,12] Interestingly, a sharp drop in diffusivity was observed on transition from the low temperature monoclinic phase to the high temperature tetragonal phase, highlighting the link between the unique modulated crystal structure and the remarkable oxygen diffusivity in $CeNbO_{4+d}$ phases. Indeed, $CeNbO_{4+d}$ provides an interesting structural template, in which the modulation induced polyhedron distortion is correlated with enhanced oxygen diffusivity.[13]

We have recently developed materials based on the $CeNbO_{4+d}$ structural template and reported the room temperature structure and transport properties of the hyper-stoichiometric $LaNb_{0.88}W_{0.12}O_{4.06}$.[14] Its room temperature structure has distorted BO_x (B = Nb,W) polyhedra, a result of the B site cation ordering, that facilitates the difference in the charge and size between W and Nb. The distorted polyhedra form interconnected slabs along the *ac* plane,[14] while the undoped $LaNbO_4$ parent phase features isolated polyhedra.[13]

Despite great interest in the conductivity and the diffusion mechanism in $LaNb_{1-x}W_xO_{4+x/2}$ and related compounds,[9–18] their high temperature structures have been scarcely investigated. The interplay between phase transition, crystal structure and the ionic conductivity in

$LaNb_{1-x}W_xO_{4+x/2}$ has not been established, which is crucial in realizing the potential of the interstitial containing structural template. The discrepancy is likely due to the complex modulated structure, and literature reports often treated the high temperature structure as unmodulated.[15,16] Such approach risks oversimplifying the structure and missing the subtle mechanistic details relating to the oxygen diffusion process.

In this current study, the structural evolution of the $LaNb_{1-x}W_xO_{4+x/2}$ phases were investigated using high temperature diffraction-based techniques and ^{17}O and ^{93}Nb Magic Angle Spinning (MAS) Nuclear Magnetic Resonance (NMR) spectroscopy. Investigation of the high temperature crystal structure allows us to verify temperature stability of the highly defective local structure. Key structural features, including the phase transition behaviour of the $LaNb_{1-x}W_xO_{4+x/2}$ series, the distribution of the interstitial oxygen ions and the change in Nb coordination environment, were addressed using thermal analysis, *in situ* X-ray and neutron diffraction, ^{17}O and ^{93}Nb MAS NMR. The nature of the phase transitions in the $LaNb_{1-x}W_xO_{4+x/2}$ family (x = 0.04 – 0.16), and their relationship to the oxygen ion diffusion process is discussed.

2 Experimental

The materials investigated in this work were prepared using solid state synthesis from a stoichiometric mix of La_2O_3 (99.9%), Nb_2O_5 (99.9%) and WO_3 (99.9%) powders (all from Sigma-Aldrich). Before the synthesis, La_2O_3 powder was treated at 1000 °C for 10 h to remove moisture and the presence of $La(OH)_3$. All the starting powders were examined with X-ray diffraction (XRD, PANalytical X'Pert Pro MPD, Cu Kα radiation, λ = 1.54056 Å) to confirm phase purity. The powder mixtures were ball milled for 24 h in acetone with zirconia balls to achieve a homogeneous mix. The mixed powders were first calcined under an ambient atmosphere at 1200 °C for 10 h, then crushed, milled and calcined again at 1400 °C for 10 h under ambient air (all heating rate 10 °C/h). Phase purity was verified with XRD after each calcination step which was repeated for 2 to 3 times until no change in phase composition was confirmed. ^{17}O enriched $LaNbO_4$ and $LaNb_{0.86}W_{0.14}O_{4+d}$ samples were prepared by heating the as-synthesised $LaNbO_4$ and $LaNb_{0.86}W_{0.14}O_{4+d}$ in a quartz tube under 60 % ^{17}O enriched O_2 gas (Isotec, used as received) at 1000 °C in a tube furnace for 24 hours.

Thermogravimetric analysis (TGA) measurements were conducted using a Netzsch STA 449C Jupiter heat flux instrument. Approximately 50 mg of sample was loaded into a Pt crucible and

the TGA measurements were performed under static laboratory air over the temperature range of room temperature to 950 °C with a heating rate of 10 °C/min. The instrument was calibrated by measuring the empty sample environment under the same experimental conditions. Sintered, rectangular-bars with the approximate dimension 4 mm × 4 mm × 25 mm were used for dilatometry measurements, to determine the thermal expansion of the materials (Netzsch DIL 402 E dilatometer). The samples were prepared using a uniaxial press at 150 MPa followed by an isostatic press at 300 MPa for 1 min. Samples were sintered at 1400 °C for 10 h, with 10 °C/h ramp rate, and reached more than 95% density. An alumina rod reference was used to calibrate the instrument prior to sample measurement. Measurement were carried out from room temperature to 800 °C with a heating rate of 10 °C/min.

In situ neutron scattering measurements were performed at the High Resolution Powder Diffractometer (HRPD, ISIS, Rutherford Appleton Laboratories, UK). Approximately 10 g of sample was placed inside a quartz ampoule heated in a vanadium furnace. Diffraction patterns were gathered from 500 °C to 800 °C with 50 °C interval, under static air. Datasets from the high-resolution backscattered bank ($2\theta \approx 145^\circ$) in the range of 2.6 Å $\geqslant$ *d*-spacing $\geqslant$ 0.9 Å were used for the structure refinement. *In-situ* high temperature XRD (HTXRD) data were measured using a PANalytical X'Pert diffractometer (Cu $K\alpha_1$ radiation with λ = 1.54056 Å) fitted with Bühler HDK 2.4 high-temperature chamber. Samples were placed on a Pt heating strip whose temperature was controlled with joule heating. Diffraction patterns were collected from room temperature up to 800 °C with the heating rate set to 60 °C/min and a hold time of 1 min. The actual temperature of the Pt strip was calibrated by refining the lattice parameter of the Pt. All the crystal structures were refined using JANA2006.[19]

^{17}O NMR experiments on ^{17}O enriched samples were carried out on a 16.4 T Bruker Avance III spectrometer. All one-dimensional spectra were obtained with a rotor synchronized Hahn echo pulse sequence experiment with one rotor period as a dephasing delay. All isotropic resonances have been identified by recording the ^{17}O NMR spectra at two different magic angle spinning (MAS) rates minimum. Experiments in the 22 – 140 °C temperature range were performed with a Bruker 3.2 mm HXY triple-resonance MAS probe (in double resonance mode) tuned to ^{17}O at $\nu_0(^{17}O)$ = 94.96 MHz. 1D spectra were obtained with $\pi/2$ pulse length of 1.7 μs at a radio frequency field (rf) amplitude of $\nu_1(^{17}O)$ = 50 kHz. Two-dimensional triple-quantum (TQ) MAS experiments were performed with a z-filter pulse sequence.[20,21] 120 and 720 scans were averaged for each of 38 and 25 t_1 points, incremented by 70.83 μs, for ^{17}O enriched $LaNbO_4$ and $LaNb_{0.84}W_{0.16}O_{4.08}$ respectively. Hard and soft pulses were performed at rf fields

of ~ 80 kHz and ~ 8 kHz, respectively. All the samples were packed in ZrO_2 rotors and spun at a spinning frequency of ν_r = 20 kHz. Temperature calibration of the probe was performed in separate MAS experiments using the ^{207}Pb resonance of $Pb(NO_3)_2$.[22] The sample temperatures quoted subsequently have all been corrected according to this calibration and have an accuracy of ± 5 °C. Experiments at 270 °C were performed with a Bruker 4 mm X single-channel MAS probe tuned to ^{17}O at $\nu_0(^{17}O)$ = 94.96 MHz. 1D spectra were obtained with π/2 pulse length of 1.7 μs at a rf field of $\nu_1(^{17}O)$ = 50 kHz. All the samples were packed in ZrO_2 rotors and spun at a spinning frequency of ν_r = 14 kHz. Temperature calibration of the probe was performed in separate MAS experiments using the ^{79}Br resonance of KBr.[23] The sample temperatures quoted subsequently have all been corrected according to this calibration, and have an accuracy of ± 5 °C. Experiments above 270 °C were performed with a Bruker 7 mm HX laser heated[24]. MAS probe tuned to ^{17}O at $\nu_0(^{17}O)$ = 94.96 MHz. 1D spectra were obtained with π/2 pulse length of 3.3 μs at a rf field of $\nu_1(^{17}O)$ = 25 kHz. All the samples were packed in BN containers and spun at a spinning frequency of ν_r = 14 kHz in ZrO_2 rotors. Temperature calibration of the probe was performed in separate MAS experiments using the ^{79}Br resonance of KBr. The sample temperatures quoted subsequently have all been corrected according to this calibration, and have an accuracy of ± 10 °C with a temperature gradient across the BN sample holder of ~ 30 °C.

^{93}Nb NMR experiments were performed on a 20 T Bruker Avance II spectrometer using a Jeol double resonance 1 mm HX probe tuned to $\nu_0(^{93}Nb)$ = 207.90 MHz and under MAS at a spinning frequency of ν_r = 78 kHz with recycle delays of 0.1 s. One-dimensional spectra were obtained with a pulse acquire sequence experiment using selective π/2 pulse length of 2.5 μs at a rf field of $\nu_1(^{93}Nb)$ ~ 20 kHz and satisfying the weak rf regime irradiation condition. All the samples were packed in ZrO_2 rotors. TQ MAS experiments were performed with a z-filter pulse sequence and 20480 scans were averaged for each of 32 t_1 points. Hard and soft pulses were performed at rf fields of ~ 100 kHz and ~ 20 kHz, respectively. The ^{93}Nb isotropic chemical shifts and quadrupolar products were obtained from the center of gravity of the NMR lines in the TQ MAS data according to the literature.[25,26] Previous work identifying links between ^{93}Nb parameters and local structure was used for tentative spectral assignments.[27–30]

All ^{17}O shifts were externally referenced to water at 0.0 ppm. All ^{93}Nb shifts were externally referenced to $LiNbO_3$ at the center of gravity of the line at – 1003 ppm (from the known isotropic shift of this phase of – 988 ppm[30] and a quadrupolar-induced shift[31] calculated to be

15 ppm at the 20 T magnetic field used for ^{93}Nb) which corresponds to the primary reference of saturated K[$NbCl_6$] in CH_3CN at 0 ppm. NMR data were processed using the MatNMR package implemented within MatLab.

3 Results and Discussion

Thermal Analysis

Thermogravimetric Analysis (TGA)

The mass change of the $LaNb_{1-x}W_xO_{4+x/2}$ (x = 0.04 – 0.16) series, measured from room temperature to 900 °C, is plotted in Figure 1. No significant weight change from room temperature up to 900 °C was detected. A small drift of about 0.1% weight change up to 900 °C is seen in all measurements, which is mostly likely associated with instrumental effects. A weight loss of about 0.15% was observed for $LaNb_{0.96}W_{0.04}O_{4.02}$ upon heating (<50 °C) which is likely due to the loss of adsorbed water. The observation is in direct contrast to the $CeNbO_{4+d}$ system which sees a wide range of oxygen stoichiometry during heating.[32] Overall the TGA measurements suggest no detectable change in sample mass from room temperature to 900 °C, indicating good thermal stability and a stable valence state of W^{6+}.

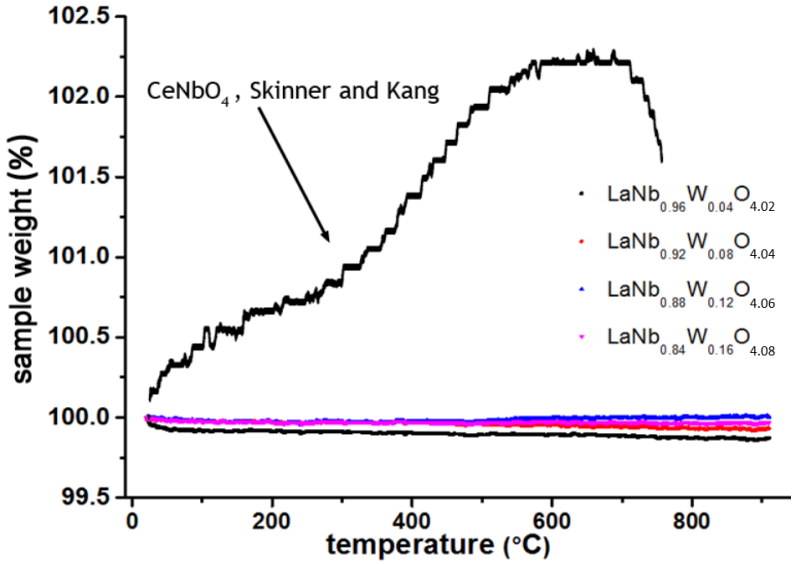

Figure 1: TGA measurement of various $LaNb_{1-x}W_xO_{4+x/2}$ (x = 0.04 – 0.16) samples from room temperature to 800°C under laboratory air. The data for $CeNbO_4$ from Skinner and Kang is listed for comparison.[32]

Dilatometry

Dilatometry curves of the $LaNbO_4$ reference, as well as the W doped $LaNb_{1-x}W_xO_{4+x/2}$ compositions, recorded in the temperature range from 200 °C to 900 °C, are shown in Figure

2. For the undoped $LaNbO_4$, two distinct regions, corresponding to the low temperature monoclinic phase and the high temperature tetragonal phases respectively, are well separated. A sharp decrease in the thermal expansion rate was observed and is attributed to the monoclinic (*m*) to tetragonal (*t*) phase transition.[33] The phase transition temperature was determined by first extrapolating the linear part of the expansion curve (the red lines in Figure 2a), and then finding the intersection between the low and high temperature regions. The phase transition temperature (T_{tr}, reported in Table 1) was estimated to be 490 ± 10 °C for the undoped $LaNbO_4$ which is in good agreement with the literature.[33,34]

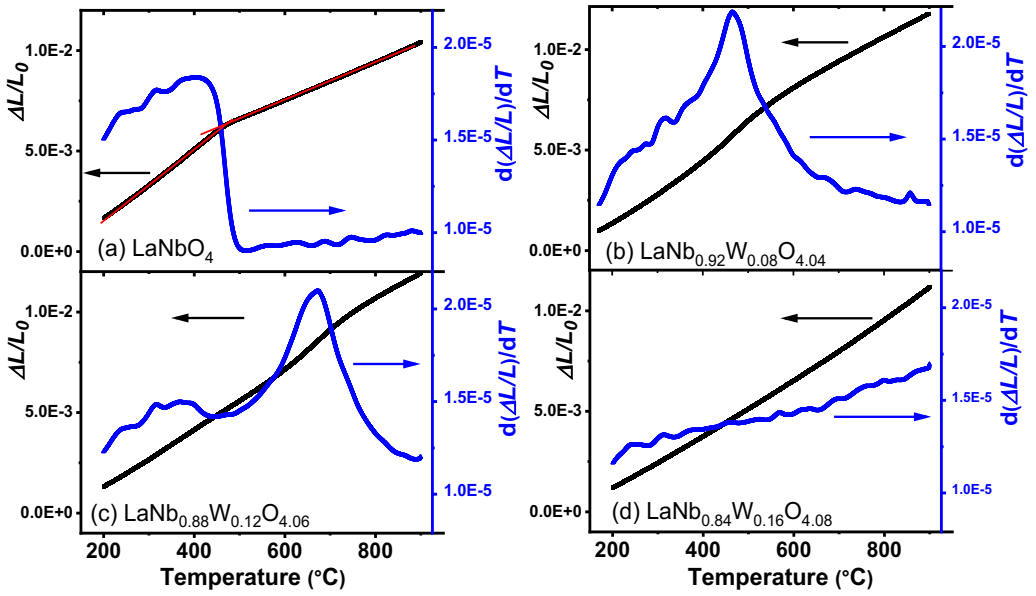

Figure 2: Dilatometry curves show the length change and the linear expansion rate as a function of temperature for (a) $LaNbO_4$ and various $LaNb_{1-x}W_xO_{4+x/2}$ compounds with (b) x = 0.08 (c) x = 0.12 and (d) x = 0.16. The phase transition in $LaNbO_4$ was determined from the intercept of the linear part of the expansion curve, highlighted by the red lines in (a).

The thermomechanical behaviour of $LaNb_{1-x}W_xO_{4+x/2}$ compositions, however, is more complicated; instead of a sudden decrease of the thermal expansion rate approaching the phase transition, the change in $LaNb_{0.92}W_{0.08}O_{4.04}$ and $LaNb_{0.88}W_{0.12}O_{4.06}$ was less abrupt (Figure 2b and c). For samples with 8 at% to 12 at% W dopant, the thermal expansion rate increased gradually before reaching a transition point, after which a slow decrease in the expansion rate was observed. Such a transition was absent in $LaNb_{0.84}W_{0.16}O_{4.08}$ (Figure 2d). The thermal expansion coefficients (TECs, reported in Table 1), before and after the transition, were obtained by averaging the length change of the samples over the respective temperature regions. Comparing with the $LaNbO_4$ parent phase, the W dopant reduces the discrepancy in TEC between the low and high temperature regions (reported in Table 1). For fuel cell applications, a sudden change in TEC promotes mismatch between the electrolyte and electrode during the

start-up stage and thus often leads to mechanical failure;[35] dilatometry results therefore suggest improved mechanical stability of the $LaNb_{1-x}W_xO_{4+x/2}$ electrolyte with W substitution. In addition, the TEC of the $LaNb_{1-x}W_xO_{4+x/2}$ phases are higher than the conventional electrolyte (i.e. the TEC of $Ce_{0.9}G_{0.1}O_{2-d}$ is ~12 × 10^{-6}/K from room temperature to 800°C[36]) and has a closer match with conventional electrodes such as $La_{0.6}Sr_{0.4}Co_{0.2}Fe_{0.8}O_{3-d}$ (LSCF) of 16.6 × 10^{-6}/K from room temperature to 650 °C[37] indicating that the $LaNb_{1-x}W_xO_{4+x/2}$ phases have suitable mechanical properties to function in fuel cells.

Table 1: Thermal expansion coefficients of the $LaNbO_4$ and various $LaNb_{1-x}W_xO_{4+x/2}$ compositions determined from dilatometry measurements shown in Figure 2.

Composition	TEC high temperature (10^{-6}/K)	TEC low temperature (10^{-6}/K)	T_{tr} (°C)	references
$LaNbO_4$	17.3	9.3	490 ± 10	this work
	17.3	7.1	510 ± 10	[11]
	14.0	8.4	504 ± 10	[12]
$LaNb_{0.92}W_{0.08}O_{4.04}$	17.5	12.7	468 ± 5	this work
$LaNb_{0.88}W_{0.12}O_{4.06}$	16.2	13.1	669 ± 5	this work
$LaNb_{0.84}W_{0.16}O_{4.08}$	14.5		-	this work

High Temperature XRD of the $LaNb_{1-x}W_xO_{4+x/2}$ (x = 0.04 – 0.16) Series

The evolution of the structure and the phase transition of $LaNb_{1-x}W_xO_{4+x/2}$ (x = 0.04–0.16) materials from room temperature to 850 °C was investigated using *in situ* high temperature X-ray diffraction. The complexity of the phase transition behaviour is well illustrated by the $LaNb_{0.88}W_{0.12}O_{4.06}$ composition (Figure 3): at room temperature, this composition has a (3 + 2)D modulated structure, with a monoclinic parent phase, indicated by the satellite peaks in the diffraction pattern. Increasing the temperature lowers the intensity of these satellite peaks. At 500 °C, the modulation reflections (the position of the modulation peak with the highest intensity is marked with an arrow in Figure 3) were still observable, whereas the parent structure seems to have transformed to tetragonal symmetry. *In situ* neutron diffraction data indicate that the satellite peaks become indistinguishable from the background between 650 °C and 800 °C (Figures S1 & S2 in the supporting information). At 800 °C, an unmodulated high temperature tetragonal phase formed, similar to the high temperature parent structure of $LaNbO_4$.

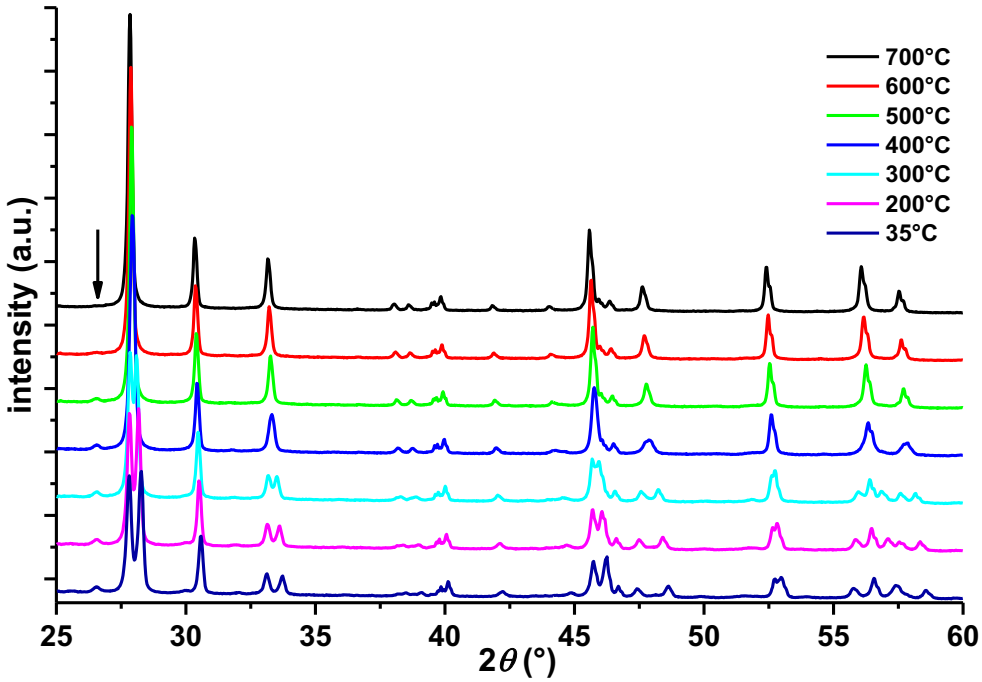

Figure 3: Selected high temperature XRD patterns for the $LaNb_{0.88}W_{0.12}O_{4.06}$ phase; the position of the satellite reflection with highest intensity is highlighted by the arrow.

The lattice parameters of the $LaNb_{0.88}W_{0.12}O_{4.06}$ composition, obtained using the Le Bail method, are plotted in Figure 4. The subscript "*m*" and "*t*" indicate the monoclinic and tetragonal structure respectively. The b_m axis was chosen as the unique axis for the monoclinic phase which coincides with the c_t axis in the tetragonal unit cell. This choice of unique axes is consistent with the previous report, and aims to avert confusion.[38] Approaching the phase transition temperature, T_{tr}, a_m decreases while c_m increases, resulting in the merging of the monoclinic symmetry-related peaks in the XRD pattern consistent with a transformation to tetragonal symmetry. The b_m increases almost linearly with temperature, while the β angle decreases gradually and becomes 90° above the transition temperature.

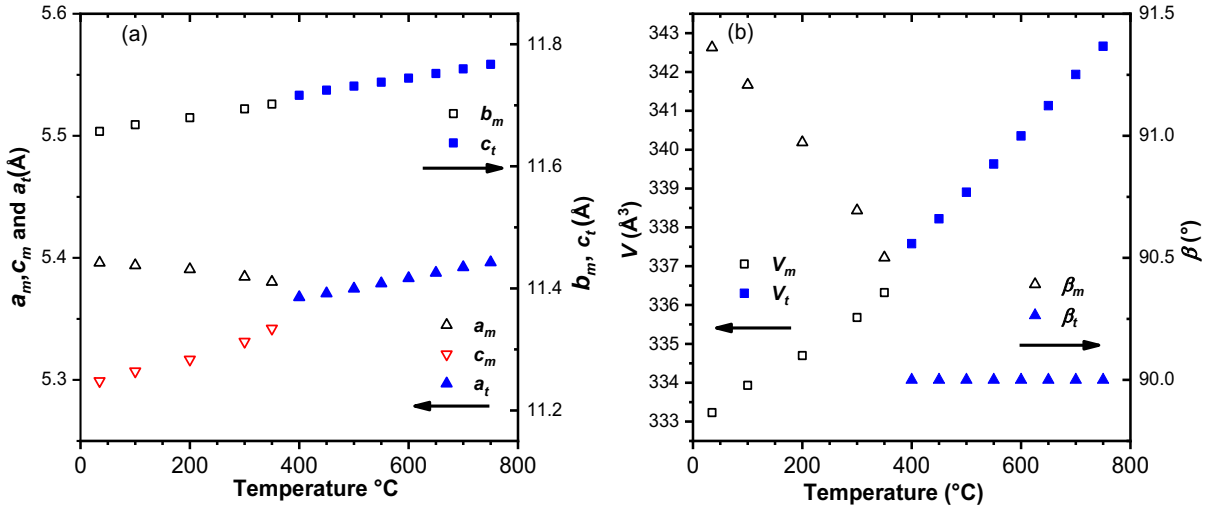

Figure 4: Refined lattice parameters (a) and cell volume (b) of the $LaNb_{0.88}W_{0.12}O_{4.06}$ composition as a function of temperature from the X-ray data shown in Figure 3. Error bars are smaller than the symbols. The subscripts "*m*" and "*t*" refer to the monoclinic and tetragonal structures respectively.

The *m* to *t* transition temperature of the parent phase varies with the W dopant concentration. For instance, neutron scattering data indicates that increasing the dopant level (W = 16 at%) sees a tetragonal-monoclinic mix at room temperature, where the tetragonal phase dominates (Figures S3 & S4), whereas the $x = 0.04$ composition has a phase transition temperature closer to the undoped $LaNbO_4$ phase (Figure S5). Based on the HTXRD data at least three phases, namely a modulated monoclinic phase, a modulated tetragonal structure and an unmodulated tetragonal phase, have been identified.

In situ neutron scattering of $LaNb_{1-x}W_xO_{4+x/2}$

In Situ Neutron Scattering of $LaNb_{0.88}W_{0.12}O_{4.06}$

The HTXRD study clearly identified various structural polymorphs, although detailed structural information, such as atomic position, especially the interstitial position, could not be obtained due to the limitations of instrument resolution and insensitivity to oxygen scattering. The structure of $LaNb_{0.88}W_{0.12}O_{4.06}$ was therefore examined using *in situ* high-resolution neutron scattering, in the temperature range 500 °C to 800 °C. This temperature range is of interest as the HTXRD result hinted at a phase transition between a modulated and an unmodulated tetragonal phase.

The neutron scattering pattern of $LaNb_{0.88}W_{0.12}O_{4.06}$ recorded at 500 °C in static air was first refined with only the unmodulated scheelite phase ($I4_1/a$, space group 88). Site occupancy of all the elements were fixed according to the nominal composition when refining the lattice parameters, atomic position and atomic displacement parameters (ADPs). Constraints on the occupancy were released in the final refinement, although the Nb/W ratio was still fixed at 88 at%/12 at% at the B site. No significant deviation from ideal stoichiometry was observed and therefore nominal stoichiometry was used for the subsequent data analysis. The refinement of the parent structure finally converged to $R_p = 0.028$ and $R_{wp} = 0.032$. Visual inspection of the refined pattern however revealed additional peaks (insert in Figure S6), whose position coincides with the satellite reflections, therefore confirming the presence of superstructure at elevated temperature. These peaks were not observed by the in-house HTXRD and are possibly related to long-range oxygen ordering. The structural modulation had to be addressed before the interstitials could be investigated as both superstructure and the interstitial content contribute to the observed intensity at the peak position in the parent phase.[39]

To refine the modulated structure, the superspace group (SSG) $I4_1/a(\alpha, \beta, 0)00(-\beta, \alpha, 0)00$ was used, based on the space group of the parent structure. There were other SSGs available which are derived from same parent group however the other choices all have a modulation component along the unique axis (c_t), which is inconsistent with the modulation waves in the low temperature structure.[40] The chosen SSG was also used in the literature to refine the (3 + 2)D modulated $Na_{2/7}Gd_{4/7}MoO_4$ scheelite[41] and $CaEu(MoO_4)_4$.[42]

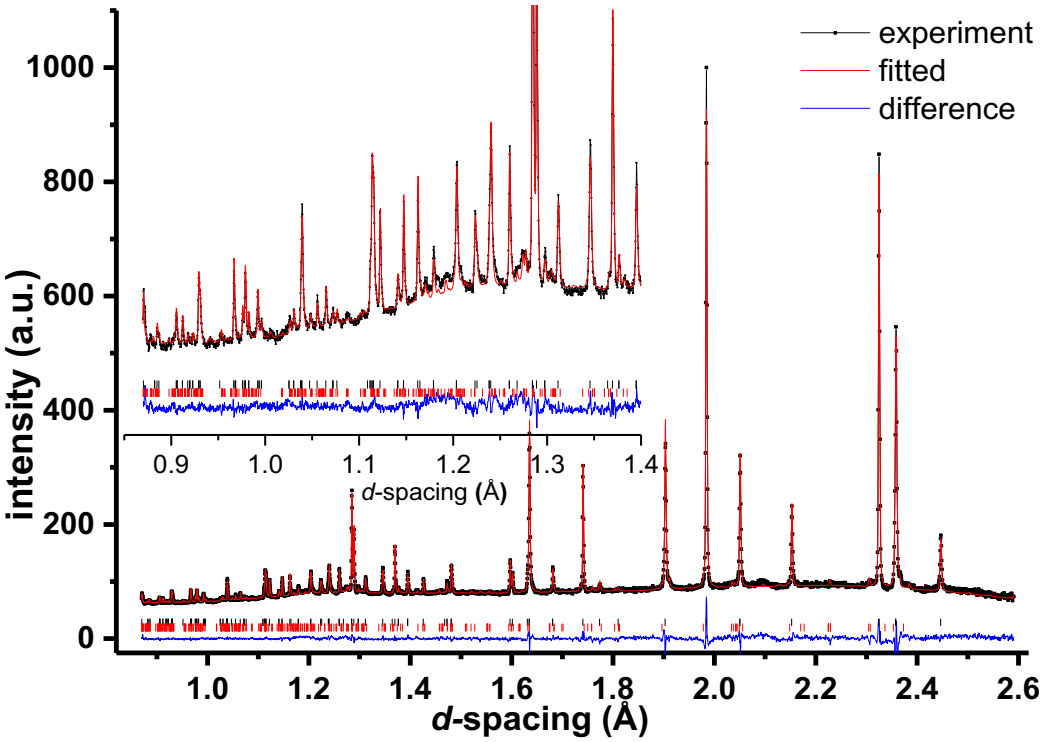

Figure 5: Rietveld refinement of neutron powder scattering data of the $LaNb_{0.88}W_{0.12}O_{4.06}$ composition recorded at 500 °C using the SSG $I4_1/a(\alpha, \beta, 0)00(-\beta, \alpha, 0)00$. Improved fitting with R_p = 0.022 and R_{wp} = 0.023 were obtained, by including the structural modulation in the model. Black, red and blue lines show the experimental data, modelled data and the difference plot respectively. The black ticks mark the theoretical Bragg peak position. The inset shows the enlarged pattern in the *d*-spacing of 0.84 Å to 1.40 Å range.

Table 2: Summary of the experimental conditions for the *in situ* neutron data of $LaNb_{0.88}W_{0.12}O_{4.06}$ at 500 °C

Composition	$LaNb_{0.88}W_{0.12}O_{4.06}$
Space group	$I4_1/a(\alpha, \beta, 0)00(-\beta, \alpha, 0)00$
Temperature	500 °C
a b c (Å)	5.37466(8) 5.37466(8) 11.72917(18)
V (Å^3)	338.821(9)
modulation waves	$\boldsymbol{q_1} = 0.3033(3)\boldsymbol{a}^* + 0.1177(4)\boldsymbol{b}^*$
	$\boldsymbol{q_2} = -0.1177(4)\boldsymbol{a}^* + 0.3033(3)\boldsymbol{b}^*$
data collection	
instrument	HRPD at ISIS
data range	*d* = 2.5889 Å to 0.8696 Å
resolution	$\Delta d/d = 4 \times 10^{-4}$
Reflections (all/observed)	1173/758
among them,	
Main Reflections (all/observed)	119/9
1st order (all/observed)	1045/639
R, R_w for Bragg reflections (R_{all})	7.2%, 5.9%
among them,	
Main Reflections (R, R_w)	3.7%, 4.1%
$\boldsymbol{q_1}$ 1st order (R, R_w)	12.3%, 6.5%
$\boldsymbol{q_2}$ 1st order (R, R_w)	11.7%, 6.6%
R_p, R_{wp}	2.2%, 2.3%

To refine the modulated phase, the q modulation vectors and the Fourier magnitudes of the low temperature $LaNb_{0.88}W_{0.12}O_{4.06}$ structure was used as the input for the subsequent refinement. Only first order modulation waves were refined as most higher order reflections had intensity lower than the 3σ detection limit. Nb and W were set to have identical fractional coordinates, ADP and displacive modulation amplitude were refined based on the site and geometry constraints. The magnitude of the modulation waves was initially fixed at 0.2, which was later released during the final stage of the refinement. The 748 observed peaks allowed the refinement of 33 independent parameters, including the anisotropic displacement parameters. The refinement finally converged with $R_p = 0.022$ and $R_{wp} = 0.023$. The refined pattern is shown in Figure 5, and the experimental parameters, the refined atomic positions and the modulation magnitude are summarized in Tables 2-4 respectively.

Table 3: Summary of the refined atomic parameters of the average structure reported in Figure 5.

	Occ.	*x*	*y*	*z*	U_{11}	U_{22}	U_{33}	U_{12}	U_{13}	U_{23}
La	0.997(12)	0	0.25	0.625	0.0397(12)	0.0397(12)	0.0176(13)	0	0	0
Nb/W	0.88/0.12	0	0.25	0.125	0.0356(14)	0.0356(14)	0.0390(01)	0	0	0
O	1.005(8)	0.2407(4)	0.0910(3)	0.0414(2)	0.0544(14)	0.0690(01)	0.0382(10)	0.0150(1)	0.0088(11)	0.0230(13)
Cation site	Bond length (Å)						Bond valence sum (BVS)			
La	2.503(2) Å × 4, 2.546(2) Å × 4						3.1(1)			
Nb/W	1.835(2) Å × 4, 2.973(2) Å × 4						5.0(1)			

Table 4: Refined Fourier magnitudes for the $LaNb_{0.88}W_{0.12}O_{4.06}$ phase at 500 °C.

site		*x*	*y*	*z*
La	position	0	0.25	0.625
	s,1[a]	0	0	-0.0030(7)
	c,1	-0.0123(15)	0.0220(11)	0
	s,2	0	0	0.0032(6)
	c,2	0.0220(11)	-0.0123(15)	0
Nb/W	position	0	0.25	0.125
	s,1	0	0	0.0088(8)
	c,1	-0.0076(16)	0.0218(13)	0
	s,2	0	0	-0.0088(8)
	c,2	-0.0218(13)	-0.0076(16)	0
	p_{c1}, p_{c2}[b]		-0.25(6), -0.25(6)	
O	position	0.240(1)	0.092(3)	0.042 (1)
	s,1	-0.0008(18)	0.0043(16)	0.0031(7)
	c,1	-0.0022(19)	0.0334(15)	0.0036(7)
	s,2	-0.0001(15)	-0.0040(2)	-0.0034(7)
	c,2	-0.0289(13)	-0.0143(19)	0.0021(8)
	Distance (Å)	average	min	max
	La-O	2.533	2.462	2.572
	Nb-O	1.832	1.772	1.902

[a] s, c stands for Fourier magnitude of sin and cos wave respectively; the number describes the wave vectors: the 1st wave is along $\boldsymbol{q_1}$ direction and the 2nd wave is along $\boldsymbol{q_2}$ direction.

[b] $p = p_0 + p_{c1}\cos(2\pi t) + p_{c2}\cos(2\pi u)$, in which p_o is the site occupancy of the parent structure. p_{c1}, p_{c2} are the Fourier magnitude for the occupational waves; *t,u* are the coordinates in the internal axes; both the Fourier magnitude of the displacive and the occupational waves. The slightly negative occupancy might be related to the choice of wavefunction, similar to that reported in ref[14,41]

The nuclear density and the residual density maps, in the vicinity of the Nb and La sites, were examined (Figure 6). Overall, the residual density is about 1–2% of the observed density, indicating good fitting quality.

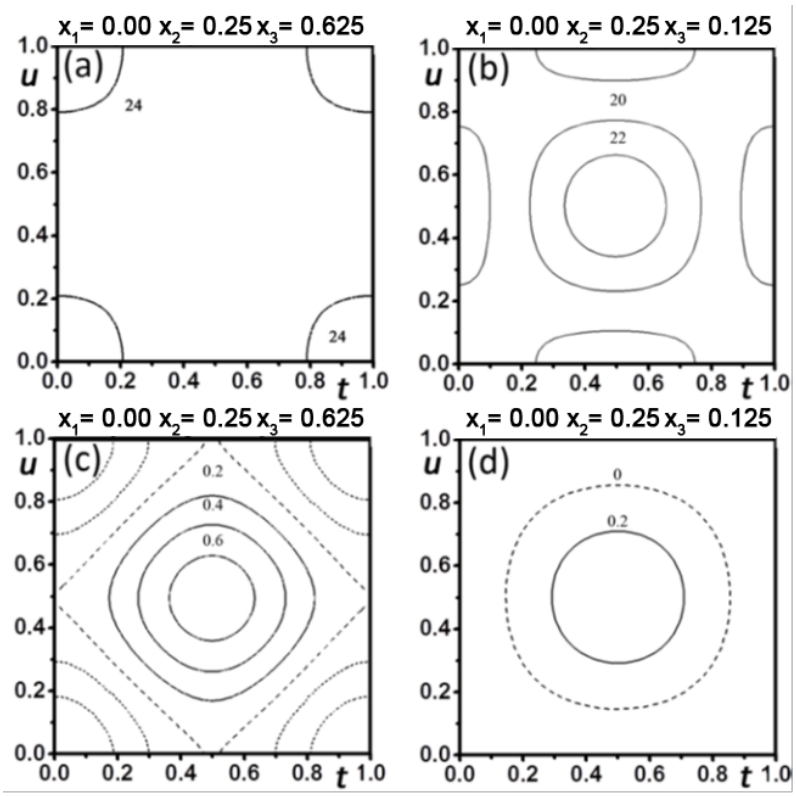

Figure 6: Observed nuclear density maps in the vicinity of (a) La and (b) Nb; and the corresponding difference nuclear density maps in (c) and (d), as a function of the internal coordinates. The contour in (a) and (b) is 2 fm Å^{-3} whereas in (c) and (d) is 0.2 fm Å^{-3}. Overall a residual level approximately 1-2% of the observed nuclear density was registered.

When refining the structure at 650 °C, the fitting quality improved little with the inclusion of structural modulation (R_{wp} from 0.024 to 0.023, Figure S1). Unresolved intensity, such as the features between 1.19 Å and 1.27 Å, was observed. These modulation peaks become quite broad with increasing temperature (Figure S2) and potentially correspond to a partially ordered local structure and mark the transition between the modulated structure and disordered tetragonal parent phase. Closer examination of the local structure however is necessary to verify the existence of any intermediate phase. The degradation in the signal to noise ratio makes fitting with the modulated structural model less reliable; the refinement was nevertheless attempted using a (3 + 2)D structural model for the 650 °C pattern and the fitting is reported in the supplemental information (Figure S1). Increasing the temperature sees further reduction of the peak intensity, and no satellite reflections were observed at 800 °C. The high resolution neutron scattering data is in good agreement with the HTXRD (Figure 3), and confirmed a modulated phase at 500 °C, which gradually transforms into the disordered high temperature tetragonal parent phase.

In Situ Neutron Scattering of $LaNb_{0.84}W_{0.16}O_{4.08}$

The same procedures described in the previous section were used to refine the structure of $LaNb_{0.84}W_{0.16}O_{4.08}$. Unlike the $LaNb_{0.88}W_{0.12}O_{4.06}$ composition, which goes through a phase transition from a modulated structure to an unmodulated structure between 650 °C to 800 °C, neutron scattering data confirmed that the $LaNb_{0.84}W_{0.16}O_{4.08}$ composition maintains its modulated structure up to 800 °C. All the diffraction patterns could be refined using the same $I4_1/a(\alpha, \beta, 0)00(-\beta, \alpha, 0)00$ SSG. In Figure 7, the data recorded for the $LaNb_{0.84}W_{0.16}O_{4.08}$ phase at 800 °C is shown, highlighting the stability of the structural modulation.

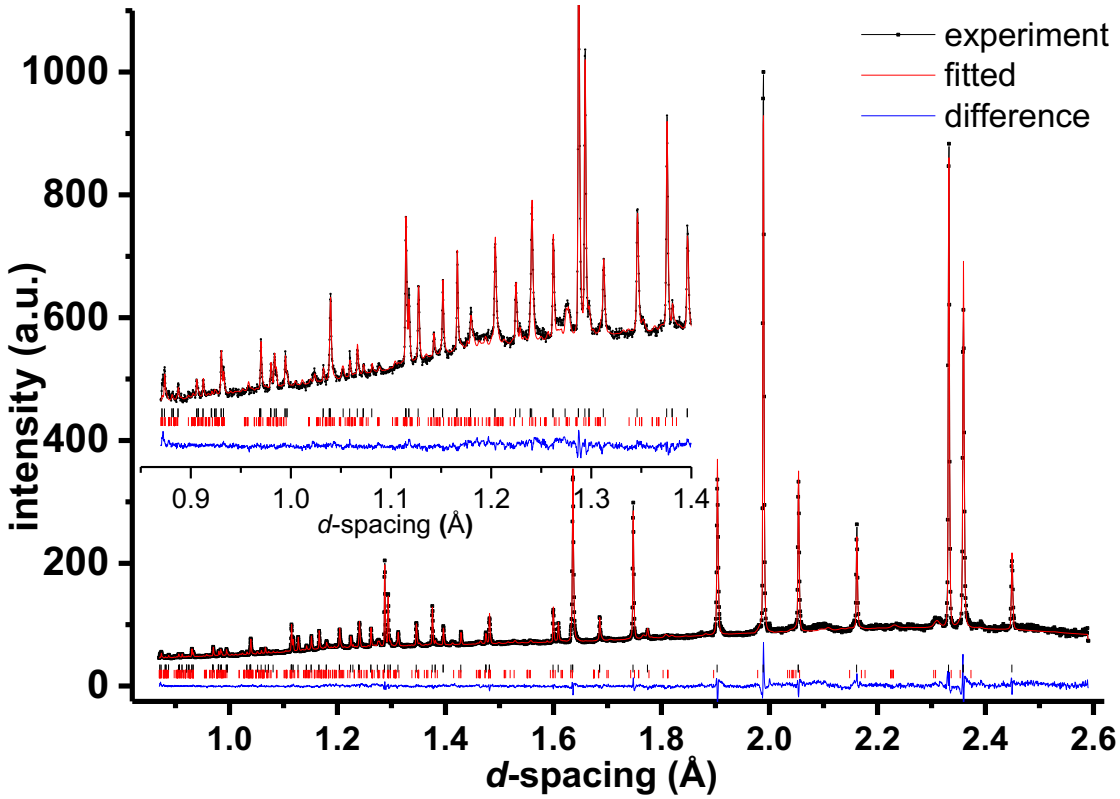

Figure 7: Rietveld refinement of neutron powder diffraction data for $LaNb_{0.84}W_{0.16}O_{4.08}$ recorded at 800 °C, using the SSG $I4_1/a(\alpha, \beta, 0)00(-\beta, \alpha, 0)00$. Good fitting with R_p = 0.022 and R_{wp} = 0.023 were obtained. Black, red and blue lines show the experimental data, modelled data and the difference plot respectively. The black and red vertical lines mark the theoretical peak position of the parent structure and the modulated peaks respectively. The inset shows the enlarged pattern in the 0.84 Å to 1.40 Å range.

When refining the occupancy modulation of W/Nb, the occupational wave magnitudes of the x = 0.12 composition was used as an input. The refinement showed little improvement of the fitting (R_p changed from 0.022 to 0.0217), while a large negative occupancy (<-0.8) in the *t-u* section was observed, making the model physically unrealistic. The occupational modulation therefore was fixed at 0.2 and -0.2 respectively for Nb and W for the refinement of the entire neutron scattering dataset for the x = 0.16 composition. Data with better quality (preferably

single crystal diffraction data), is required to allow for higher order modulation reflections to be resolved.

Interstitial Position in $LaNb_{0.84}W_{0.16}O_{4.08}$

The role of the interstitial oxygen ion during the conduction process has been highlighted with previous experimental[10,43] and DFT atomic simulation.[15] While the correlated interstitialcy diffusion is proposed to explain the long-range oxygen transport in the hyper-stoichiometric scheelite compounds,[15] the interstitial oxygen position in these compounds has been elusive. Indeed, no specific site was identified when examining the difference density map of the $LaNb_{0.84}W_{0.16}O_{4.08}$ at 500 °C in our study: the observed residual density is at the same level as the negative density, and was therefore ascribed to noise (Figure S8).

In fact, the reported interstitial positions in the hyper-stoichiometric scheelite structures are scattered due to high oxygen mobility coupled with the low interstitial concentration.[43] For instance, when studying the modulated $CeNbO_{4+d}$ phases, Thompson *et al.* suggested that the interstitial occupied the empty eight-coordinate site, at (0, 0.25, 0.375) (marked by red spheres in Figure 8), which leads to minimal disturbance to the neighbouring ions.[44] A different Wyckoff 8*e* position in $I4_1/a$ space group at (0, 0.25, 0.325) was predicted in La doped $PbWO_4$ by Takai *et al.*[43] The authors pointed out that the refined occupancy is only 1/3 of the expected value, and suggested that the interstitial could occupy other 8*e* positions with varied *z* coordinate (along the arrow direction shown in Figure 8). Most recently, Pramana *et al.*[13] proposed the location of oxygen interstitial not at a specific crystallographic position in the parent structure, but at normal lattice oxygen site in an expanded unit cell. Both the "interstitial" and lattice oxygen cooperatively contribute to diffusion. The structure is therefore better described as $Ce_{12}Nb_{12}O_{51}$, highlighting the similarity between the lattice and the "interstitial" oxygen.[13]

Refinement of the interstitial position in $LaNb_{0.84}W_{0.16}O_{4.08}$ was attempted following the methodology proposed in ref,[43] which assumed an interstitial locating at (0, 0.25, *z*), however no satisfactory result was obtained. The constraints on the interstitial position were later released, and the refinement converged with the interstitial oxygen ion occupying the (0.274, 0.104, 0.223) general position. However, the refinement returned a large negative occupancy which indicates a false local minimum and was therefore discarded.

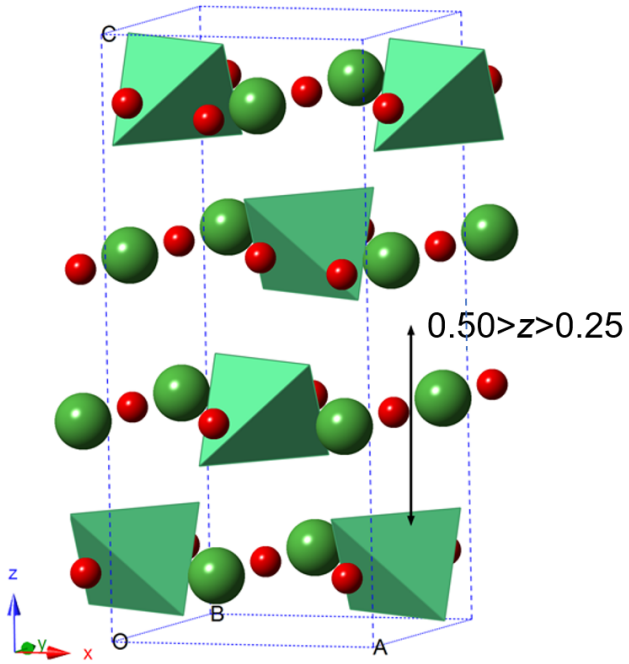

Figure 8: Proposed interstitial (shown as red spheres) positions in $LaNb_{0.84}W_{0.16}O_{4.08}$ based on ref.[30] and [28]. The green sphere represents La^{3+} ion whereas the Nb/W atoms are shown in the polyhedral form. The interstitial is assumed to be located along (0, 0.25, z), shown by the black arrow.

It is possible that the interstitial oxygen assumes a rather diffuse distribution in the $LaNb_{0.84}W_{0.16}O_{4.08}$ system at 500 °C and the oxygen ions are delocalized along the conducting pathway leading to a reduced occupancy at any particular crystallographic site, and thus minimal residual density. Alternatively, the interstitial might be modulated due to the cation ordering, as the ordering of the anion network is expected from the cation ordering.[5,13,45,46]

In both cases, a diffuse distribution of the interstitial oxygen is predicted. Such prediction is consistent with most recent reports on apatite-type germanates,[6,47,48] which showcased the oxygen interstitial delocalised along the diffusion migration pathway. There have been earlier reports on the apatite,[4] melilite[49] and fergusonite/scheelte[15,43,50] which predicts localized interstitial sites. Although these reports focus on the structure at room temperature whereas the mobility of oxygen is expected to increase with increasing sample temperature as suggested by the high temperature ^{17}O NMR data of $LaNb_{0.84}W_{0.16}O_{4.08}$ (see below). It should also be recognized that charge compensation with A and B site vacancies is possible which would further reduce the interstitial content in $LaNb_{1-x}W_xO_{4+x/2}$.[51]

Observation of Nb Environment with Coordination Larger Than Four

A number of ^{93}Nb solid state NMR studies have identified trends linking the ^{93}Nb parameters with niobium coordination number and other structural parameters,[27–30] as for many other nuclei and cations (for example, ^{27}Al),[52] and is exploited here to probe the local structure of Nb in $LaNb_{0.92}W_{0.08}O_{4.04}$. Although the ^{93}Nb nucleus is very receptive owning to its large gyromagnetic ratio and 100% natural abundance, its large quadrupolar moment introduces a dominant 2nd-order quadrupolar broadening of the central transition. This can be reduced to provide improved resolution by using very high magnetic fields and applying very fast MAS rates and all ^{93}Nb spectra in this work were obtained at 20 T under MAS at 78 kHz.

The one dimensional ^{93}Nb spectrum of $LaNbO_4$ is given in Figure S9a, and displays the expected broad and complex pattern which is in fair agreement with the simulated spectrum obtained by using known NMR parameters obtained from a comprehensive multi magnetic field strengths study under non spinning conditions.[30] The TQMAS spectrum of this phase (Figure S9a) reveals a single niobium crystallographic site at a shift of ~ -1200 ppm and a TQMAS shift of ~ -640 ppm (Figure 9) that yields an isotropic chemical shift of ~ -850 ppm, in agreement with the literature value of -853 ppm[30] and a coordination number of 4 for Nb.

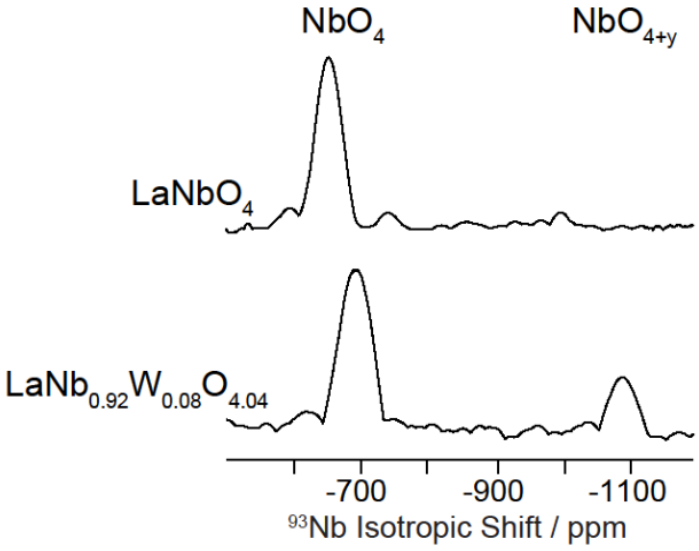

Figure 9: Projection of the isotropic dimension of the ^{93}Nb TQ MAS NMR spectrum of $LaNbO_4$ and $LaNb_{0.92}W_{0.08}O_{4.04}$ (Figure S9) obtained at room temperature at 20 T and under a MAS rate of 78 kHz. The position of the Nb site in tetrahedral symmetry (NbO_4) and tentatively attributed to niobium environment (NbO_{4+y}, y > 1) with coordination larger than four are also show.

The ^{93}Nb very fast MAS NMR spectrum of $LaNb_{0.92}W_{0.08}O_{4.04}$ (Figure S9b) shows multiple overlapping peaks in the -500 -1600 ppm region with fewer spinning sidebands than $LaNbO_4$. Interestingly, the ^{93}Nb TQMAS spectrum demonstrates that in addition to the 4-coordinated

niobium site present in $LaNbO_4$ (observed here at an isotropic chemical shift of ~ -780 ppm in agreement with the -714 and -853 ppm range expected for NbO_4 polyhedral found in the literature[27–30]), a second site with a highly distorted lineshape close to axial symmetry can be observed with a TQMAS shift of ~ -1100 ppm (Figure 9) at an isotropic chemical shift of ~ -1100 ppm. Importantly, the lower shift of this resonance than for the 4-coordinated niobium site, supported by the known general trend for the ^{93}Nb shifts to decrease with increasing niobium coordination numbers,[27–30] would suggest that this signal corresponds to a coordination number larger than 4 and may therefore be tentatively ascribed to niobium environments near interstitial oxygen ions, possibly in five- or six-coordinated niobium polyhedra.

Phase Diagram of the $LaNb_{1-x}W_xO_{4+x/2}$

Based on the analysis presented so far, the Nb rich corner of the $LaNbO_4$-$LaWO_{4.5}$ phase diagram is tentatively proposed in Figure 10. The solid lines in the phase diagram indicate the single-phase boundary; the dotted line separates the monoclinic and tetragonal parent phase, whereas the dashed line is the boundary between the modulated structure and the unmodulated structure. The peak temperatures of the thermal expansion rate from the dilatometry measurements (Figure 2) are also marked on the phase diagram.

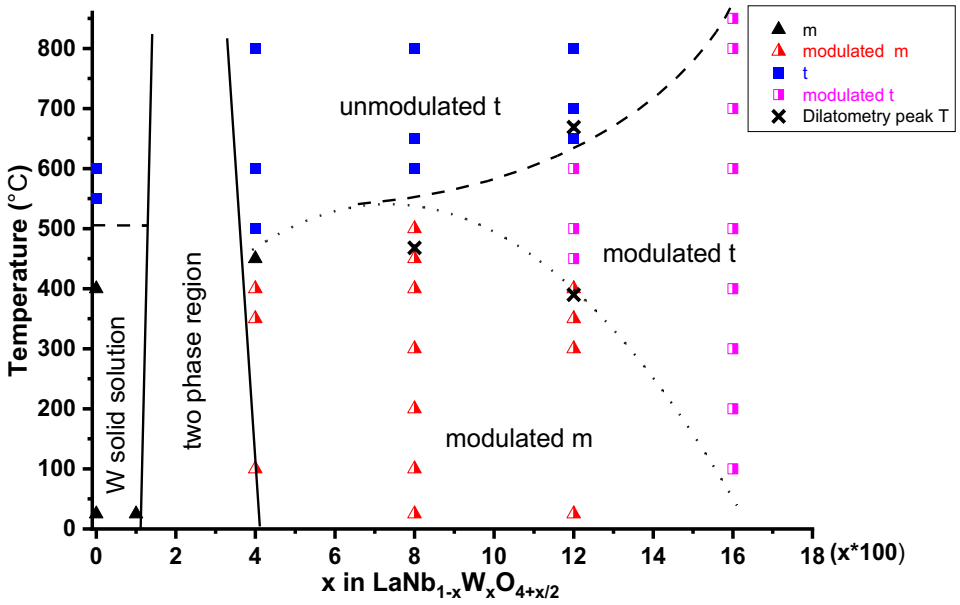

Figure 10: Proposed phase diagram of the $LaNb_{1-x}W_xO_{4+x/2}$ system, highlighting the complexity of the system. The solid lines signify the boundaries between a biphasic region and the single-phase region. The dotted line is based upon the transition temperature reported in Table S1 and separates the phases with monoclinic and tetragonal parent structures; the dashed line marks the separation between the modulated phases and the unmodulated structure. All lines are guides for the eye. The "peak" temperatures from the expansion rate reported in Figure 2 are marked as "x" on the proposed phase diagram.

The first interesting observation in this phase diagram is the correlation between the "peak" temperature during dilatometry and the phase transition temperature obtained from diffraction. For instance, the expansion rate of the $LaNb_{0.88}W_{0.12}O_{4.06}$ composition first peaked at ~390 °C and later at ~670 °C (Figure 2c), which corresponds well with two-phase transition of the x = 0.12 composition. In addition, no abrupt change of shrinkage rate was observed in the $LaNb_{0.84}W_{0.16}O_{4.08}$ composition (Figure 2d), which coincides with the absence of a phase transition in this composition. Such correlation however is missing in $LaNb_{0.92}W_{0.08}O_{4+d}$, as the dilatometry peak temperature is about 50-70 °C below the modulated to disordered transition. Still, it is not unreasonable to assume that the modulated to disordered phase transition would affect the thermal expansion of the material. As demonstrated earlier,[14] the Nb/W-O local environment of the modulated $LaNb_{0.88}W_{0.12}O_{4.06}$ phase differs significantly from its parent structure.

When varying the temperature, both the magnitude and the direction of the $\boldsymbol{q}$ vectors are expected to change,[53] leading to variations of bond lengths and bond angles in addition to the thermal effect. The accumulation of the change would, on a macroscopic scale, perturb the expansion rate. In analogy to the ferroelastic to paraelastic transition of the parent $LaNbO_4$ structure, it is logical to assume that the impact of modulation on the linear expansion rate will be at an extremum when the order-disorder transition occurs. Indeed, the peak temperatures of the dilatometry seem to coincide with the transition temperatures between the modulated structure and unmodulated structure in $LaNb_{1-x}W_xO_{4+x/2}$ (Figure 10); it is therefore speculated that the removal of the structural modulation would introduce a subtle change in the expansion behaviour; however further experiments are required to verify this conjecture.

Theories of the modulated phase transition have been devised to explain the transition between the high temperature incommensurate phase and the low temperature commensurate structure (normally referred to as the "lock-in phase", often observed below room temperature)[54–56] and have provided great assistance in understanding the phase transition in structures with charge density wave ordering and magnetic ordering.[57–59] However, the phase transition in modulated structures at elevated temperature has been overlooked. The proposed phase diagram highlights the complexity of structural variation in the modulated system and calls for future investigation.

Capturing the Local Oxygen Structure with ^{17}O MAS NMR Spectroscopy

^{17}O solid state NMR was used to provide further insights into the local oxygen environment and the oxide ion mobilities of these complex crystal structures. Due to the very low natural

abundance of ^{17}O (0.037 %), the only NMR active isotope of oxygen, both $LaNbO_4$ and $LaNb_{0.84}W_{0.16}O_{4.08}$ samples were enriched in ^{17}O by a gas solid exchange reaction with ^{17}O enriched O_2 gas at 1000 °C prior to acquisition of the ^{17}O NMR data. The XRD powder patterns (Figure S10) are similar to the ones obtained for the parent $LaNbO_4$ and $LaNb_{0.84}W_{0.16}O_{4.08}$ materials showing that the additional heat treatment in the ^{17}O gas at 1000 °C did not affect the crystal structures.

The ^{17}O MAS NMR spectrum of ^{17}O enriched $LaNbO_4$ is shown in Figure 11 (and Figure S11 for full spectral width) and displays two well separated resonances at 442 (~1.5 kHz broad) and 564 (~1.3 kHz) ppm with an approximately 1:1 intensity ratio (along with a number of spinning sidebands arising from the satellite transitions of this spin 5/2 nucleus), in agreement with the two oxygen crystallographic sites O1 and O2 in monoclinic $LaNbO_4$. The shorter bond distance between Nb and O2 (1.844 Å) than between Nb and O1 (1.903 Å) yields a larger chemical shielding surrounding the O2 sites than for the O1 sites and therefore a smaller shift of the O2 site (442 ppm) than for the O1 sites (564 ppm). The ^{17}O TQMAS experiment[21] (which enables isotropic spectra, i.e. free of anisotropic broadening, of quadrupolar nuclei such as ^{17}O to be obtained) is given in Figure 12 and allows isotropic chemical shift values of 442 and 564 ppm for the O2 and O1 oxygen sites to be determined. These values are identical to the resonance peak positions given above, implying that virtually no quadrupolar couplings are present and demonstrating that the NMR lines are dominated by chemical shift interactions and not second-order quadrupolar broadenings as anticipated for ionic solids. In this case, the spinning sideband envelope spreads over approximately 3000 ppm (or 270 kHz at 16.7 T) at room temperature and reflects the large ^{17}O chemical shift anisotropy (and estimated to be ~ - 1300 ppm).

The high temperature MAS ^{17}O NMR spectra are presented in Figure 11 and were obtained under different MAS rates as different NMR probes were used depending on the required temperature and the MAS NMR probe capabilities (see experimental section for further details). Upon increasing the temperature to about 500 °C under MAS, both Nb-O1 and Nb-O2 resonances of monoclinic $LaNbO_4$ phase converge almost linearly (at a rate of ~0.07 ppm/°C for Nb-O1 and ~0.14 ppm/°C for Nb-O2) towards a value of ~520 ppm (close to the average shift value for the Nb-O1 and Nb-O2 peaks at 503 ppm). Extrapolation of the data between room temperature and 500 °C yields an anticipated convergence to occur at ~560 °C which is in agreement with the ^{17}O MAS NMR spectrum collected at 605 °C that reveals a single broad resonance at ~515 ppm (with a spinning sideband manifold covering ~1200 ppm). This

temperature-dependent gradual change of the NMR shifts in monoclinic $LaNbO_4$ is induced by the second-order phase transition between the low temperature monoclinic and high temperature tetragonal phase in rare earth niobates (about 495-520 °C in $LaNbO_4$).[60] The observation of a single ^{17}O resonance at 605 °C is in agreement with the unique crystallographic oxygen site of the tetragonal phase.

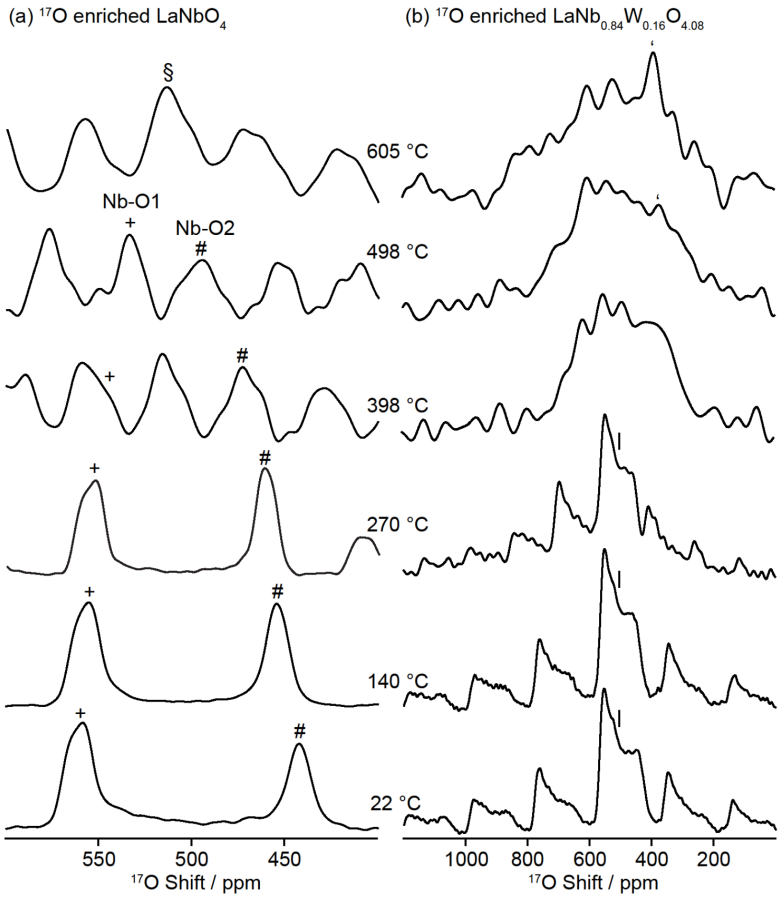

Figure 11: Variable temperature ^{17}O MAS NMR spectrum of (a) ^{17}O enriched $LaNbO_4$ and (b) ^{17}O enriched $LaNb_{0.84}W_{0.16}O_{4.08}$ obtained at 16.4 T. The samples temperatures are given next to each spectrum. The MAS rate ν_r was 22, 14 and 4 kHz in the 22-140 °C, 270 °C and 398-605 °C temperature range, respectively (see the experimental section for further details). In (b), the lower MAS rate used to record the spectra above 300 °C explains the broadening of the spectra above its temperature due to the overlapping of the central transition with the spinning sidebands. The isotropic resonances are marked with # and + in monoclinic $LaNbO_4$ (for O2 and O1, respectively), § in tetragonal $LaNbO_4$ and | in $LaNb_{0.84}W_{0.16}O_{4.08}$. Symbol ‘ indicates natural abundance ^{17}O signal from the ZrO_2 rotor (around 380 ppm).[52] All other peaks are spinning sidebands.

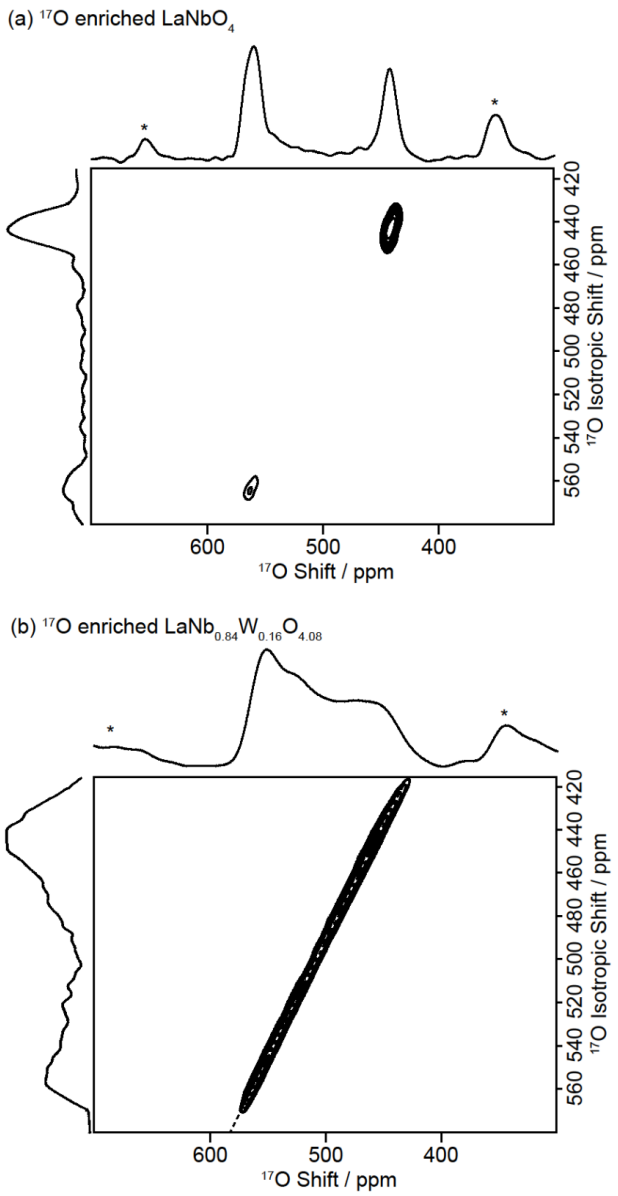

Figure 12: ^{17}O Triple Quantum MAS NMR spectrum of (a) ^{17}O enriched $LaNbO_4$ and (b) ^{17}O enriched $LaNb_{0.84}W_{0.16}O_{4.08}$ obtained at room temperature at 16.4 T and under a MAS rate of 20 kHz. The dashed line in (b) indicates the + 1 diagonal. Asterisk (*) denote spinning sidebands.

The room temperature ^{17}O NMR spectrum of ^{17}O enriched $LaNb_{0.84}W_{0.16}O_{4.08}$ obtained under MAS rate of 22 kHz (Figure 11b) is dramatically different from the one obtained for $LaNbO_4$ revealing a very broad resonance (~13 kHz) centred at ~500 ppm (along with a range of broad spinning sidebands, see Figure S11). This resonance spreads from 420 to 570 ppm covering the positions of the two ^{17}O resonances of Nb-O1 and Nb-O2 in $LaNbO_4$ and therefore consistent with a large range of Nb-O/W-O bond lengths ranging from ~1.844 to 1.903 Å in $LaNb_{0.84}W_{0.16}O_{4.08}$ (corresponding to Nb-O2 to Nb-O1 in $LaNbO_4$). The broad centerband at ~500 ppm therefore reflects a distribution of chemical shifts rather than second-order quadrupolar broadening. This is in agreement with both the ^{17}O TQMAS spectrum of this

material (Figure 12b) which shows that the signal at ~500 ppm is clearly spread along the +1 diagonal and with the presence of broad spinning sidebands that should be narrowed by MAS if no distribution of chemical shift was present. There is no clear ^{17}O NMR signal for the interstitial oxygen, and the data above suggest that a range of oxygen environments are observed instead and correspond to different Nb-O and W-O bond lengths and local environments. Upon sample heating, disappearance of the spinning sidebands starting at 270 °C indicates the onset of slow motion in $LaNb_{0.84}W_{0.16}O_{4.08}$ (see supporting information for further details) and is in sharp contrast with the large number of sidebands in the $LaNbO_4$ data (Figures 11 and S12), likely indicating enhanced oxygen ion mobility in the former phase. Above 300 °C, restriction of the maximum MAS rate available on the 7 mm laser heated MAS probe (4 kHz) does not allow the central transition to be clearly observed due to overlapping spinning sidebands and resulting in a broad pattern ($\approx$ 63 kHz at 605 °C).

4 Conclusion

In this contribution, the structure evolution of the $LaNb_{1-x}W_xO_{4+x/2}$ series from room temperature up to 800 °C is investigated. Using high temperature thermal analysis, *in situ* diffraction techniques and ^{17}O and ^{93}Nb MAS NMR, a sequence of transformation in $LaNb_{1-x}W_xO_{4+x/2}$ between a modulated monoclinic phase, a modulated tetragonal phase and an unmodulated tetragonal phase has been revealed. *In situ* scattering experiments shed light on the structural evolution of the $LaNb_{0.88}W_{0.12}O_{4.06}$ and $LaNb_{0.84}W_{0.16}O_{4.08}$ compositions: modulation peaks were observed and the structure of the $LaNb_{0.88}W_{0.12}O_{4.06}$ composition between 500 °C and 650 °C was successfully refined using the $I4_1/a(\alpha,\beta,0)00(-\beta,\alpha,0)00$ superspace group. The $LaNb_{0.84}W_{0.16}O_{4.08}$ composition, on the other hand, maintains its modulated structure till 800 °C. Attempts were made to pinpoint the position of the interstitial oxygen in the $LaNb_{0.84}W_{0.16}O_{4.08}$ composition at 500 °C, and ^{93}Nb MAS NMR data suggests the presence of a distorted site tentatively ascribed to Nb near an interstitial ion. The refinement suggests a non-localized distribution of the interstitial oxygen that agrees with the distribution of ^{17}O shifts observed in the MAS NMR spectra. It is possible that an extended structural model that incorporates interstitials as lattice ions is required to fully describe the structure. Based on the diffraction and thermal analysis data, the phase diagram of the $LaNb_{1-x}W_xO_{4+x/2}$ is drawn, which highlights the complex transitions between a modulated monoclinic phase, a modulated tetragonal phase and a disordered tetragonal.

5 Acknowledgements

The authors acknowledge funding from the EPSRC for a studentship to R.D.B., the EU Marie Curie actions for an International Incoming Fellowship 2011-2013 (grant 275212) to F.B., Clare Hall at the University of Cambridge for a Research Fellowship to F.B., the EU ERC for an Advanced Fellowship (LIBNMR) to C.P.G. We thank Matthew T. Dunstan for recording the XRD patterns of ^{17}O enriched $LaNbO_4$ and $LaNb_{0.84}W_{0.16}O_{4.08}$. We gratefully acknowledge the Science and Technology Facilities Council (STFC) for access to neutron beamtime at HRPD, ISIS (RB1410098). The UK 850 MHz solid-state NMR Facility used in this research was funded by EPSRC and BBSRC, as well as the University of Warwick including via part funding through Birmingham Science City Advanced Materials Projects 1 and 2 supported by Advantage West Midlands (AWM) and the European Regional Development Fund (ERDF). Collaborative assistance from the 850 MHz Facility Manager (Dr. Dinu Iuga, University of Warwick) is acknowledged.

Supporting Information

Additional characterizations and data (Figures S1-S11): diffraction patterns, refined lattice parameters, Rietveld refinements, NMR spectrum. This material is available free of charge via the internet at http://pubs.acs.org.

References

(1) Huang, K.; Feng, M.; Goodenough, J. B. Synthesis and Electrical Properties of Dense $Ce_{0.9}Gd_{0.1}O_{1.95}$ Ceramics. *J. Am. Ceram. Soc.* **2005**, *81*, 357–362.

(2) Huang, K.; Tichy, R. S.; Goodenough, J. B. Superior Perovskite Oxide-Ion Conductor; Strontium- and Magnesium-Doped $LaGaO_3$: I, Phase Relationships and Electrical Properties. *J. Am. Ceram. Soc.* **2005**, *81*, 2565–2575.

(3) Lacorre, P.; Goutenoire, F.; Bohnke, O.; Retoux, R.; Lallgant, Y. Designing Fast Oxide-Ion Conductors Based on $La_2Mo_2O_9$. *Nature* **2000**, *404*, 856–858.

(4) Pramana, S. S.; Klooster, W. T.; White, T. J. Framework Interstitial Oxygen in $La_{10}(GeO_4)_5$-$(GeO_5)O_2$ Apatite Electrolyte. *Acta Crystallogr. Sect. B Struct. Sci.* **2007**, *63*, 597–602.

(5) Wei, F.; Gasparyan, H.; Keenan, P. J.; Gutmann, M.; Fang, Y.; Baikie, T.; Claridge, J. B.; Slater, P. R.; Kloc, C. L.; White, T. J. Anisotropic Oxide Ion Conduction in Melilite Intermediate Temperature Electrolytes. *J. Mater. Chem. A* **2015**, *3*, 3091–3096.

(6) Tate, M. L.; Blom, D. A.; Avdeev, M.; Brand, H. E. A.; McIntyre, G. J.; Vogt, T.; Evans, I. R. New Apatite-Type Oxide Ion Conductor, $Bi_2La_8[(GeO_4)_6]O_3$: Structure, Properties, and Direct Imaging of Low-Level Interstitial Oxygen Atoms Using Aberration-Corrected Scanning Transmission Electron Micr. *Adv. Funct. Mater.* **2017**, *27*, 1605625.

(7) Kuang, X.; Green, M. A.; Niu, H.; Zajdel, P.; Dickinson, C.; Claridge, J. B.; Jantsky, L.; Rosseinsky, M. J. Interstitial Oxide Ion Conductivity in the Layered Tetrahedral Network Melilite Structure. *Nat. Mater.* **2008**, *7*, 498–504.

(8) Magrasó, A.; Fontaine, M. L.; Larring, Y.; Bredesen, R.; Syvertsen, G. E.; Lein, H. L.; Grande, T.; Huse, M.; Strandbakke, R.; Haugsrud, R.; et al. Development of Proton Conducting SOFCs Based on $LaNbO_4$ Electrolyte - Status in Norway. *Fuel Cells* **2011**, *11*, 17–25.

(9) Packer, R. J.; Tsipis, E. V.; Munnings, C. N.; Kharton, V. V.; Skinner, S. J.; Frade, J. R. Diffusion and Conductivity Properties of Cerium Niobate. *Solid State Ionics* **2006**, *177*, 2059–2064.

(10) Esaka, T. Ionic Conduction in Substituted Scheelite-Type Oxides. *Solid State Ionics* **2000**, *136–137*, 1–9.

(11) Wachowski, S.; Mielewczyk-Gryń, A.; Zagórski, K.; Li, C.; Jasiński, P.; Skinner, S. J.; Haugsrud, R.; Gazda, M. Influence of Sb-Substitution on Ionic Transport in Lanthanum Orthoniobates. *J. Mater. Chem. A* **2016**, *4*, 11696–11707.

(12) Packer, R. J.; Skinner, S. J. Remarkable Oxide Ion Conductivity Observed at Low Temperatures in a Complex Superstructured Oxide. *Adv. Mater.* **2010**, *22*, 1613–1616.

(13) Pramana, S. S.; Baikie, T.; An, T.; Tucker, M. G.; Wu, J.; Schreyer, M. K.; Wei, F.; Bayliss, R. D.; Kloc, C. L.; White, T. J.; et al. Correlation of Local Structure and Diffusion Pathways in the Modulated Anisotropic Oxide Ion Conductor $CeNbO_{4.25}$. *J. Am. Chem. Soc.* **2016**, *138*, 1273–1279.

(14) Li, C.; Pramana, S. S.; Skinner, S. J. Room Temperature Structure and Transport

Properties of the Incommensurate Modulated $LaNb_{0.88}W_{0.12}O_{4.06}$. *Dalt. Trans.* **2019**, *48*, 1633–1646.

(15) Ferrara, C.; Mancini, A.; Ritter, C.; Malavasi, L.; Tealdi, C. Interstitial Oxide Ion Migration in Scheelite-Type Electrolytes: A Combined Neutron Diffraction and Computational Study. *J. Mater. Chem. A* **2015**, *3*, 22258–22265.

(16) Laguna-Bercero, M. A.; Bayliss, R. D.; Skinner, S. J. $LaNb_{0.84}W_{0.16}O_{4.08}$ as a Novel Electrolyte for High Temperature Fuel Cell and Solid Oxide Electrolysis Applications. *Solid State Ionics* **2014**, *262*, 298–302.

(17) Yang, X.; Fernández-Carrión, A. J.; Wang, J.; Porcher, F.; Fayon, F.; Allix, M.; Kuang, X. Cooperative Mechanisms of Oxygen Vacancy Stabilization and Migration in the Isolated Tetrahedral Anion Scheelite Structure. *Nat. Commun.* **2018**, *9*, 4484.

(18) Li, C.; Bayliss, R. D.; Skinner, S. J. Crystal Structure and Potential Interstitial Oxide Ion Conductivity of $LnNbO_4$ and $LnNb_{0.92}W_{0.08}O_{4.04}$ (Ln = La, Pr, Nd). *Solid State Ionics* **2014**, *262*, 530–535.

(19) Václav, P.; Michal, D.; Lukáš, P. Crystallographic Computing System JANA2006: General Features. *Zeitschrift für Kristallographie - Crystalline Materials*. 2014, p 345.

(20) Frydman, L.; Harwood, J. S. Isotropic Spectra of Half-Integer Quadrupolar Spins from Bidimensional Magic-Angle-Spinning Nmr. *J. Am. Chem. Soc.* **1995**, *117*, 5367–5368.

(21) Amoureux, J.-P.; Fernandez, C.; Steuernagel, S. ZFiltering in MQMAS NMR. *J. Magn. Reson. Ser. A* **1996**, *123*, 116–118.

(22) Bielecki, A.; Burum, D. P. Temperature Dependence of ^{207}Pb MAS Spectra of Solid Lead Nitrate. An Accurate, Sensitive Thermometer for Variable-Temperature MAS. *J. Magn. Reson. Ser. A* **1995**, *116*, 215–220.

(23) Thurber, K. R.; Tycko, R. Measurement of Sample Temperatures under Magic-Angle Spinning from the Chemical Shift and Spin-Lattice Relaxation Rate of ^{79}Br in KBr Powder. *J. Magn. Reson.* **2009**, *196*, 84–87.

(24) Ernst, H.; Freude, D.; Mildner, T.; Wolf, I. Laser-Supported High-Temperature MAS NMR for Time-Resolved in Situ Studies of Reaction Steps in Heterogeneous Catalysis. *Solid State Nucl. Magn. Reson.* **1996**, *6*, 147–156.

(25) Millot, Y.; Man, P. P. Procedures for Labeling the High-Resolution Axis of Two-Dimensional MQ-MAS NMR Spectra of Half-Integer Quadrupole Spins. *Solid State Nucl. Magn. Reson.* **2002**, *21*, 21–43.

(26) Ashbrook, S. E. Recent Advances in Solid-State NMR Spectroscopy of Quadrupolar Nuclei. *Phys. Chem. Chem. Phys.* **2009**, *11*, 6876–6891.

(27) Du, L. S.; Schurko, R. W.; Kim, N.; Grey, C. P. Solid-State ^{93}Nb, ^{19}F, and ^{113}Cd Nuclear Magnetic Resonance Study of Niobium Oxyfluorides: Characterization of Local Distortions and Oxygen/Fluorine Ordering. *J. Phys. Chem. A* **2002**, *106*, 7876–7886.

(28) Papulovskiy, E.; Shubin, A. A.; Terskikh, V. V.; Pickard, C. J.; Lapina, O. B. Theoretical and Experimental Insights into Applicability of Solid-State ^{93}Nb NMR in Catalysis. *Phys. Chem. Chem. Phys.* **2013**, *15*, 5115–5131.

(29) Dunstan, M. T.; Blanc, F.; Avdeev, M.; McIntyre, G. J.; Grey, C. P.; Ling, C. D. Long-Range-Ordered Coexistence of 4-, 5-, and 6-Coordinate Niobium in the Mixed Ionic-Electronic Conductor γ-$Ba_4Nb_2O_9$. *Chem. Mater.* **2013**, *25*, 3154–3161.

(30) Hanna, J. V.; Pike, K. J.; Charpentier, T.; Kemp, T. F.; Smith, M. E.; Lucier, B. E. G.; Schurko, R. W.; Cahill, L. S. A ^{93}Nb Solid-State NMR and Density Functional Theory Study of Four- and Six-Coordinate Niobate Systems. *Chem. - A Eur. J.* **2010**, *16*, 3222–3239.

(31) Baltisberger, J. H.; Gann, S. L.; Pines, A.; Wooten, E. W.; Chang, T. H.; Mueller, K. T. ^{87}Rb Dynamic-Angle Spinning NMR Spectroscopy of Inorganic Rubidium Salts. *J. Am. Chem. Soc.* **1992**, *114*, 7489–7493.

(32) Skinner, S. J.; Kang, Y. X-Ray Diffraction Studies and Phase Transformations of $CeNbO_{4+\delta}$ Using in Situ Techniques. *Solid State Sci.* **2003**, *5*, 1475–1479.

(33) Vullum, F.; Nitsche, F.; Selbach, S. M.; Grande, T. Solid Solubility and Phase Transitions in the System $LaNb_{1-x}Ta_xO_4$. *J. Solid State Chem.* **2008**, *181*, 2580–2585.

(34) Mokkelbost, T.; Lein, H. L.; Vullum, P. E.; Holmestad, R.; Grande, T.; Einarsrud, M. A. Thermal and Mechanical Properties of $LaNbO_4$-Based Ceramics. *Ceram. Int.* **2009**, *35*, 2877–2883.

(35) Singhal, S. C.; Kendall, K. *High-Temperature Solid Oxide Fuel Cells: Fundamentals, Design, and Applicatons*, 1st ed.; Elsevier B.V.: Amsterdam, 2003.

(36) Corbel, G.; Mestiri, S.; Lacorre, P. Physicochemical Compatibility of CGO Fluorite, LSM and LSCF Perovskite Electrode Materials with $La_2Mo_2O_9$ Fast Oxide-Ion Conductor. *Solid State Sci.* **2005**, *7*, 1216–1224.

(37) Xu, Q.; Huang, D.; Zhang, F.; Chen, W.; Chen, M.; Liu, H. xing. Structure, Electrical Conducting and Thermal Expansion Properties of $La_{0.6}Sr_{0.4}Co_{0.8}Fe_{0.2}O_{3-d}$-$Ce_{0.8}Sm_{0.2}O_{2-d}$ Composite Cathodes. *J. Alloys Compd.* **2008**, *454*, 460–465.

(38) Bayliss, R. D. Synthetic, Structural and Electrochemical Studies of Superstructured Rare-Earth Niobates, Ph.D. Thesis, Imperial College London, 2014.

(39) van Smaalen, S. *Incommensurate Crystallography*; Oxford University Press: Oxford, 2008.

(40) Stokes, H. T.; Campbell, B. J.; Van Smaalen, S. Generation of (3 + d)-Dimensional Superspace Groups for Describing the Symmetry of Modulated Crystalline Structures. *Acta Crystallogr. Sect. A Found. Crystallogr.* **2011**, *67*, 45–55.

(41) Morozov, V.; Arakcheeva, A.; Redkin, B.; Sinitsyn, V.; Khasanov, S.; Kudrenko, E.; Raskina, M.; Lebedev, O.; Van Tendeloo, G. $Na_{2/7}Gd_{4/7}MoO_4$: A Modulated Scheelite-Type Structure and Conductivity Properties. *Inorg. Chem.* **2012**, *51*, 5313–5324.

(42) Abakumov, A. M.; Morozov, V. A.; Tsirlin, A. A.; Verbeeck, J.; Hadermann, J. Cation Ordering and Flexibility of the BO_4^{2-} Tetrahedra in Incommensurately Modulated $CaEu_2(BO_4)_4$ (B = Mo, W) Scheelites. *Inorg. Chem.* **2014**, *53*, 9407–9415.

(43) Takai, S.; Touda, S.; Oikawa, K.; Mori, K.; Torii, S. Powder Neutron Diffraction Study of Ln-Substituted $PbWO_4$ Oxide Ion Conductors. *Solid State Ionics* **2002**, *148*, 123–133.

(44) Thompson, J. G.; Withers, R. L.; Brink, F. J. Modulated Structures in Oxidized Cerium Niobates. *J. Solid State Chem.* **1999**, *143*, 122–131.

(45) Brizé, V.; Georges, S.; Kodjikian, S.; Suard, E.; Goutenoire, F. $La_6Mo_8O_{33}$: A New Ordered Defect Scheelite Superstructure. *J. Solid State Chem.* **2004**, *177*, 2617–2627.

(46) Hadermann, J.; Perez, O.; Creon, N.; Michel, C.; Hervieu, M. The (3 + 2)D Structure of Oxygen Deficient $LaSrCuO_{3.52}$. *J. Mater. Chem.* **2007**, *17*, 2344–2350.

(47) Peet, J. R.; Chambers, M. S.; Piovano, A.; Johnson, M. R.; Evans, I. R. Dynamics in Bi(III)-Containing Apatite-Type Oxide Ion Conductors: A Combined Computational and Experimental Study. *J. Mater. Chem. A* **2018**, *6*, 5129–5135.

(48) Chambers, M. S.; Chater, P. A.; Evans, I. R.; Evans, J. S. O. Average and Local Structure of Apatite-Type Germanates and Implications for Oxide Ion Conductivity. *Inorg. Chem.* **2019**, *58*, 14853–14862.

(49) Wei, F.; Baikie, T.; An, T.; Schreyer, M.; Kloc, C.; White, T. J. Five-Dimensional Incommensurate Structure of the Melilite Electrolyte $[CaNd]_2[Ga]_2[Ga_2O_7]_2$. *J. Am. Chem. Soc.* **2011**, *133*, 15200–15211.

(50) Takai, S.; Nakanishi, T.; Oikawa, K.; Torii, S.; Hoshikawa, A.; Kamiyama, T.; Esaka, T. Neutron Diffraction and IR Spectroscopy on Mechanically Alloyed La-Substituted $PbWO_4$. *Solid State Ionics* **2004**, *170*, 297–304.

(51) Takai, S.; Sugiura, K.; Esaka, T. Ionic Conduction Properties of $Pb_{1-x}M_xWO_{4+\delta}$ (M = Pr, Tb). *Mater. Res. Bull.* **1999**, *34*, 193–202.

(52) Kenneth J.D. MacKenzie, M. E. S.; MacKenzie, K. J. D.; Smith, M. E. *Multinuclear Solid-State NMR of Inorganic Materials*, 1st ed.; MacKenzie, K. J. D., Smith, M. E., Eds.; Oxford, 2002.

(53) Bak, P. Commensurate Phases , Incommensurate Phases and the Devil ' s Staircase. *Rep. Prog. Phys.* **1982**, *45*, 587.

(54) McMillan, W. L. Theory of Discommensurations and the Commensurate-Incommensurate Charge-Density-Wave Phase Transition. *Phys. Rev. B* **1976**, *14*, 1496–1502.

(55) Grabowski, M.; Subbaswamy, K. R. Phase-Amplitude Soliton Lattice and the Lock-in Transition. *Phys. D Nonlinear Phenom.* **1982**, *5*, 348–358.

(56) Chattopadhyay, T.; Liss, K. D.; Brückel, T. Incommensurate-Commensurate Lock-in Phase Transition in $EuAs_3$. *J. Magn. Magn. Mater.* **1998**, *177–181*, 1058–1060.

(57) Chen, C.; Cheong, S.-W. Commensurate to Incommensurate Charge Ordering and Its Real-Space Images in $La_{0.5}Ca_{0.5}MnO_3$. *Phys. Rev. Lett.* **1996**, *76*, 4042–4045.

(58) Nakanishi, K.; Shiba, H. Domain-like Incommensurate Charge-Density-Wave States and the First-Order Incommensurate-Commensurate Transitions in Layered Tantalum Dichalcogenides. I. 1T-Polytype. *J. Phys. Soc. Japan* **1977**, *43*, 1839–1847.

(59) Ghiringhelli, G.; Le Tacon, M.; Minola, M.; Blanco-Canosa, S.; Mazzoli, C.; Brookes, N. B.; De Luca, G. M.; Frano, A.; Hawthorn, D. G.; He, F.; et al. Long-Range

Incommensurate Charge Fluctuations in (Y,Nd)$Ba_2Cu_3O_{6+x}$. *Science* **2012**, *337*, 821–825.

(60) Sarin, P.; Hughes, R. W.; Lowry, D. R.; Apostolov, Z. D.; Kriven, W. M. High-Temperature Properties and Ferroelastic Phase Transitions in Rare-Earth Niobates ($LnNbO_4$). *J. Am. Ceram. Soc.* **2014**, *97*, 3307–3319.

Table of Contents

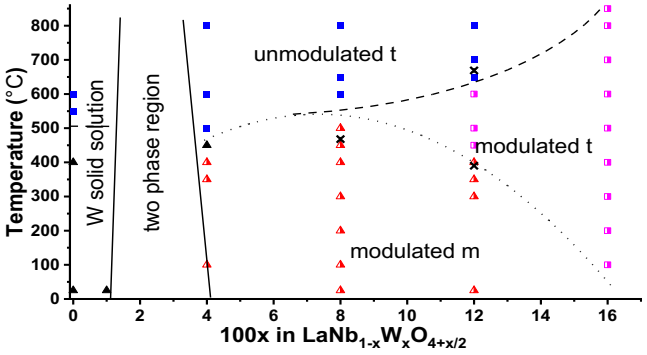

Synopsis

High temperature thermal analysis, scattering techniques and ^{17}O nuclear magnetic resonance spectroscopy reveal the structural evolution of the $LaNb_{1-x}W_xO_{4+x/2}$ (x = 0.04 - 0.16) phases to be a series of phase transitions between a modulated monoclinic phase, a high temperature unmodulated tetragonal phase and a high temperature modulated tetragonal phase.